

Experimental investigation on the vibration tuning of a shell with a shape memory alloy ring

Jie Hong^{1,2}, Wenzhong Yan¹, Yanhong Ma^{1,2}, Dayi Zhang¹ and Xin Yang³

¹ School of Energy and Power Engineering, Beihang University, No. 37 Xueyuan RD. Haidian Dist., Beijing 100191, People's Republic of China

² Co-Innovation Center of Advanced Aero-Engine, Haidian Dist., Beijing 100191, People's Republic of China

³ Beijing Power Machineries Institute, Fengtai Dist., Beijing 100074, People's Republic of China

E-mail: mayanhong@buaa.edu.cn

Received 30 April 2015, revised 2 July 2015

Accepted for publication 17 July 2015

Published 8 September 2015



CrossMark

Abstract

This paper presents a new design of a smart ring with motion actuators made of a shape memory alloy (SMA). The mechanical properties of the SMA actuator were investigated at room (25 °C) and high (90 °C) temperatures to better understand its characteristics. The results show that the smart ring with an SMA not only shows good stability and rapid effectiveness in the vibration control of the test shell, but observably eliminates the nonlinear vibration characteristics due to contact and rubbing between the ring and shell during the heating process. The smart ring also shows excellent performance in the isolation of transient vibration resulting from impact or random loads. With regard to impact loads, the response peak value can reduce by 57.4% in most cases, while the value is 38.7% for random excitations. The study shows the feasibility of using the SMA material for potential applications of vibration tuning the casings of aero-engines.

Keywords: vibration tuning, shell, smart ring, shape memory alloy, recovery force

(Some figures may appear in colour only in the online journal)

1. Introduction

The tendency for designing thin-wall casings for modern aero-engines contributes to the mode frequency's dense and geometric nonlinearity. It is difficult for these shells to completely avoid resonance in actual operating conditions with unpredicted excitation loads, which may lead to cracks, deformation or fatigue fractures on the casing. At the same time, the excitation transmitted from the rotor will cause vibration of the casing and its connection structures. It is necessary to efficiently control the vibration of the casing and prevent the vibration from transmitting further. Therefore, the effective vibration control of casings under broadband, complicated, and nonlinear excitation is one of the key issues of aero-engine design.

There are currently several techniques for achieving vibration control [1]; passive control, active control, and semi-active control. Passive control, which possesses high

reliability, is widely applied in practice [2–8]. For example, Abbas *et al* [9] adopted granular damping technologies with metal swarf to suppress vibrations in a hollow aluminum beam. However, this is limited in the control of complex vibrations due to its narrow controllable frequency range. Another technique used is active control. There are several devices that can achieve active control, such as the active variable system (AVS) [10] and the active support system (ASS) [11], and they have better effects and adaptability than passive control. Unfortunately, the requirements of active control for external power and control procedures may prevent its application for complex vibration situations. Another candidate is the semi-active control technique, which assimilates the remarkable effect of active control and the high reliability of passive control. Mass and damping control systems [12], the variable stiffness control system [13, 14] and variable dampers [15] which require intelligent sensors and drivers, are the most common semi-active controls [1].

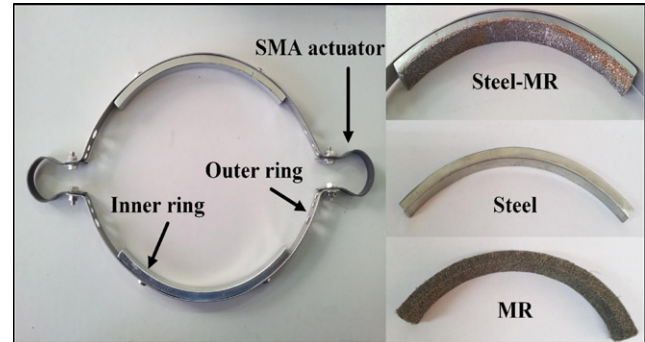
By manufacturing them into smart devices, smart materials satisfy the requirements of semi-active control and achieve effective monitoring and control of the vibration. Shape memory alloy (SMA) is one of these smart materials and is extensively used on account of its excellent mechanical properties [16–20].

Arne Ölander first discovered an SMA in 1932 [21]. The importance of shape memory materials was not recognised until William Buehler and Frederick Wang revealed the shape memory effect in a nickel–titanium alloy in 1962 [22]. Ever since then, the demand for SMAs has been growing in numerous fields, such as structures and composites [23], automotive [24], and aerospace [25–28]. Yuse *et al* [29] controlled the vibration of a cantilevered beam by taking advantage of the recovery force characteristic of SMAs. Suzuki and Kagawa [30] utilized the H-infinity theory to control the vibration of a cable made of an SMA. Chen [31] used the classical algorithm for linear optimal control to drive the SMA wires of solar panels. Zhang *et al* [32] and Ma *et al* [33] made SMA wires into metal rubber (MR) and focused on the dynamic mechanical behavior of MR in vibration control. In addition, austenitic SMA exhibits hyperelastic characteristics, which are utilized to design various kinds of dampers with excellent performance [34, 35]. However, previous work mainly focuses on the microstructures and the analysis of the phase transformation of threadlike SMA materials, and pay less attention to performance tests of the macro-mechanical characteristics of large-sized SMA materials [36–41], and no attempt has been made to evaluate the potential of the smart ring as a platform for shell semi-active control applications. The work presented in this paper aims at understanding the feasibility of using SMA smart ring devices with big recovery forces using temperature as a control parameter, with a series of tests carried out on a custom test rig.

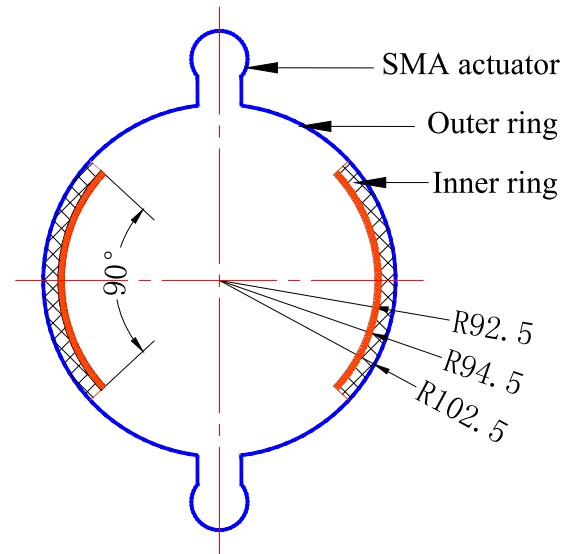
2. Description of the SMA smart ring

Figure 1 shows the structures and components of the SMA smart ring with SMA actuators made from $Ti_{50}Ni_{41}Cu_9$ [42]. The outer ring acts as a frame to connect both the inner ring and the SMA actuator by bolts. The SMA actuators contribute to the power part and generate the mechanical recovery force applied on the shell through deformation which can be controlled by thermal loading. The inner ring is a ninety degree arc comprised of one thick steel sheet and one thin MR [43–46] sheet. The dimensions of the smart ring are shown in figure 1(b). In order to study the influence of the structure of the inner rings on the mechanical behaviors of the shell and to verify the validity of the steel–MR inner ring, two additional different inner rings were built, namely a steel inner ring and an MR inner ring, which have the same overall size as the steel–MR inner ring.

The vibration tuning mechanism of the SMA smart ring can be described as reinforced constraining layer damping [47–49]. Once the SMA actuators are heated, the SMA smart ring generates a contracting stress on the shell, leading to a stiffness increment in the shell, thus the vibration of the shell



(a) The structure of the SMA smart ring



(b) The dimensions of the smart ring

Figure 1. Diagram of the SMA smart ring. (a) The structure of the SMA smart ring. (b) The dimensions of the smart ring.

is suppressed [50, 51]. At the same time, the constraining layer damping structure comes into action since the MR sheet (damping layer), which is a kind of high damping material [52–54], is sandwiched between the shell and the steel plate (constraining layer). As a result, the vibration energy dissipation mechanism of the SMA smart ring is achieved by dry friction energy dissipation through the shear deformation of the MR sheet. In the same manner, the transient vibration of the shell resulting from an impact or random loads can be isolated, benefiting from the contraction and damping of the smart ring.

The manufacture of the SMA actuators can be summarized as two steps, namely heat setting and two-way shape memory training (see figure 2). The SMA plates have a length of 110 mm, a width of 10 mm and a thickness of 1 mm, and the distance between the two holes as shown in figure 2(a) is 90 mm. The SMA plates were forced into a U-shape by distorting and fastening them with special tooling. The U-shaped plates obtained were heated at 500 °C for 60 min and then cooled to room temperature. After heat setting, the distance between the two holes was 20 mm and would not vary anymore. Finally, two-way shape memory training was carried

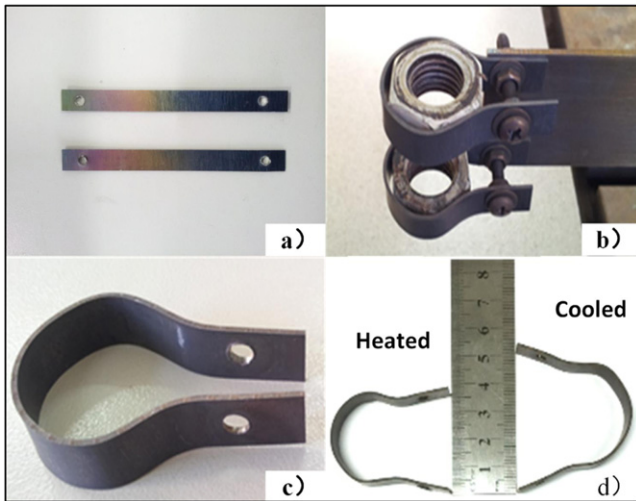


Figure 2. Scheme of the manufacture process of the SMA actuators. (a) SMA plates; (b) the SMA plates are mechanically fixed into a U-shape; (c) heat setting the U-shaped SMA plate; (d) two-way shape memory training.

out on the U-shaped plates and repeated 50 times to acquire a stable variation (14 mm) for the distance of the two holes between the heating and cooling process, i.e. 32 mm for heating and 46 mm for cooling. The transformation temperature of the $\text{Ti}_{50}\text{Ni}_{41}\text{Cu}_9$ SMA was obtained by differential scanning calorimetry (DSC-Setaram Instrumentation, labSys Evo). The DSC analysis was carried out using a heating rate of $10^\circ\text{C min}^{-1}$. The results of the thermal analysis are shown in figure 3.

3. Quasi-static test of the SMA actuator

The quasi-static test of the SMA actuator was carried out on the test rig shown in figure 4. The actuator was assembled on an Instron machine (WDW3100 made by the China Changchunxin Company) with a special clamping tool, to ensure that the actuator would not suffer any preload at the beginning, and as a result, the distance of the two holes is 46 mm before the experiment. In addition, the test rig is equipped with a temperature control system and force transducer. The temperature control system is made of a proportional-integral-derivative (PID) temperature controller and quartz lamps which provide heat that changes the temperature of the SMA actuators. Furthermore, in order to make sure that the actuator is heated equally, an insulated enclosure with heat-insulated cotton and two pieces of mica board is used. The temperature of the SMA actuators can reach 90°C when heated, and cooling to room temperature is achieved by shutting off the heat source. The recovery force of the actuator is obtained by the force transducer (measuring range: 0–7.5 kN). The test was repeated several times to study the stability of the actuator recovery force over time.

The results of the first seven cycles of the experiment are shown in figure 5. It is worth noting that the recovery force can reach a high level while the size of the actuator is limited,

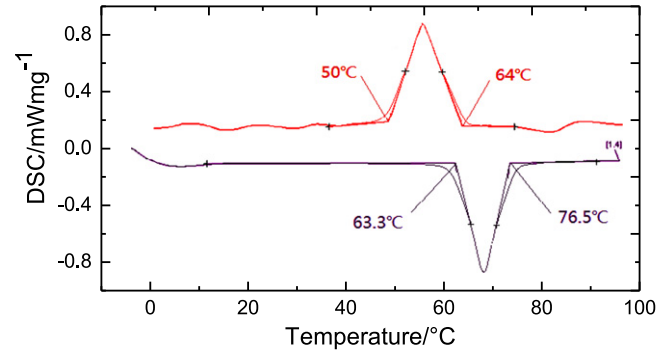


Figure 3. DSC curves for the shape memory alloy.

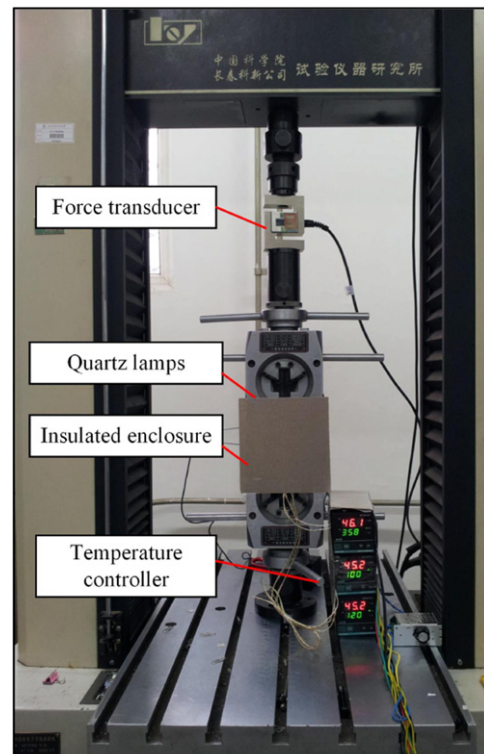


Figure 4. Quasi-static test rig for the SMA actuator.

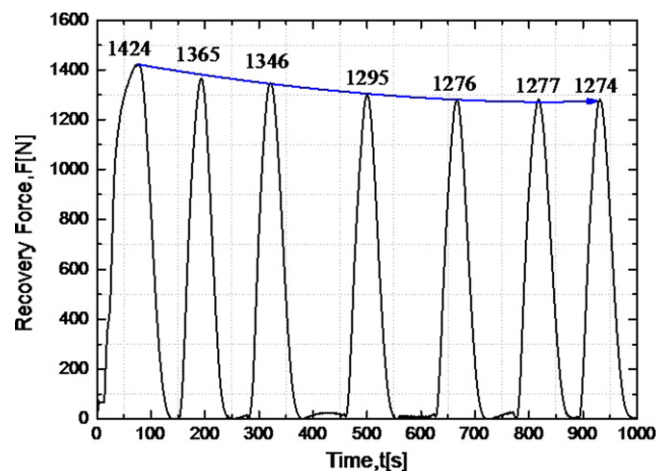


Figure 5. Time history curve for the recovery force of an SMA actuator.

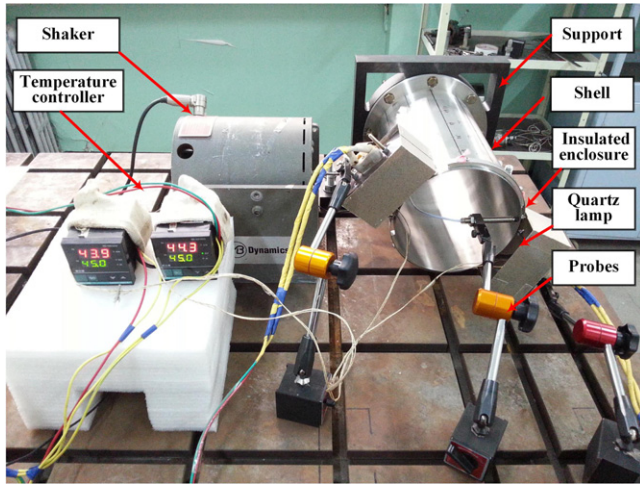


Figure 6. Test rig for the shell with SMA smart ring.

mostly because of the special U-shaped design of the SMA actuator. The value of the recovery force tends to quickly stabilize at 1280 N with a slight decrease, showing good stability of the actuators, which guarantees the consistency of all of the experiments.

4. Shell test experimental setup

The shell test rig includes a support, the test shell (size: ϕ 185 \times 300 \times 1 mm), soft springs, the SMA smart ring, the vibration measurement unit, and a temperature control system, which is the same as that used in the quasi-static test of the SMA actuator (figure 6). The shell is cantilevered and fixed on a rigid support by its fixture fringe on one side, while the other side is fitted with the SMA smart ring by using soft springs to keep the ring separated from the shell at room temperature. Moreover, the smart ring is installed without a preload, which means that the distance between the two holes in the SMA actuator is 46 mm, the same as in the quasi-static test. One more thing to note is that the position of the smart ring is fixed for the course of the whole experiment, as represented in figures 6 and 7. A shaker (Model 50 made by MB Dynamics) is equipped to excite the shell at spot E

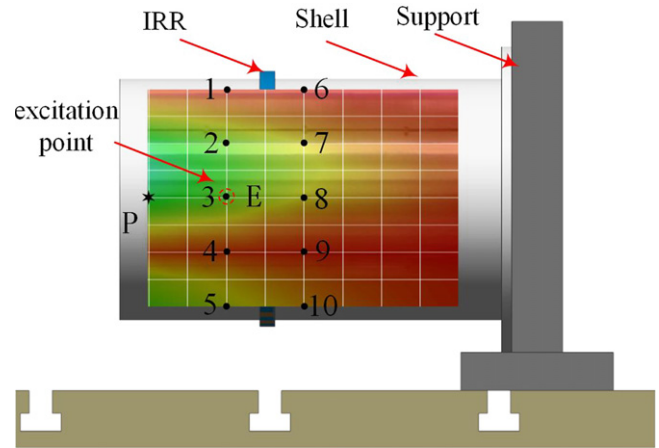


Figure 8. Distribution of measure points.

opposite point 3 (shown in figure 8 as \star). The vibration amplitude of the shaker is controlled through the shaker amplifier (SL500VCF made by MB Dynamics) ranging between 0.01 and 0.2 mm (peak to peak), and the excitation frequency is controlled by a signal generator (DG1022 made by RIGOL).

The displacement of the shell is mainly measured by a scanning vibrometer (PSV-400, made by Polytec) set up on the ground, as shown in figure 7. The vibrometer is used to detect the signal of multiple points on the shell synchronously by setting lots of measuring points in a net format (see figure 8). The point P (shown as \star) in the middle of the left boundary of the net is the main point for measurement during the vibration response control experiment. An eddy current motion probe (3300XL 5/8 mm made by Bently, sensitivity of 7.87 V mm^{-1}), magnetically fixed on the foundation, is arranged at point P inside the shell for the modal experiment.

In addition, during the vibration isolation experiment, ten points (shown as \bullet in figure 8) evenly distributed along 180 degrees of the circumference are picked up. Points 3 and 8 are at the same position circumferentially as the midpoint of the inner ring. However, points 1, 5, 6 and 10 are out of the range of the inner ring in the circumferential direction.

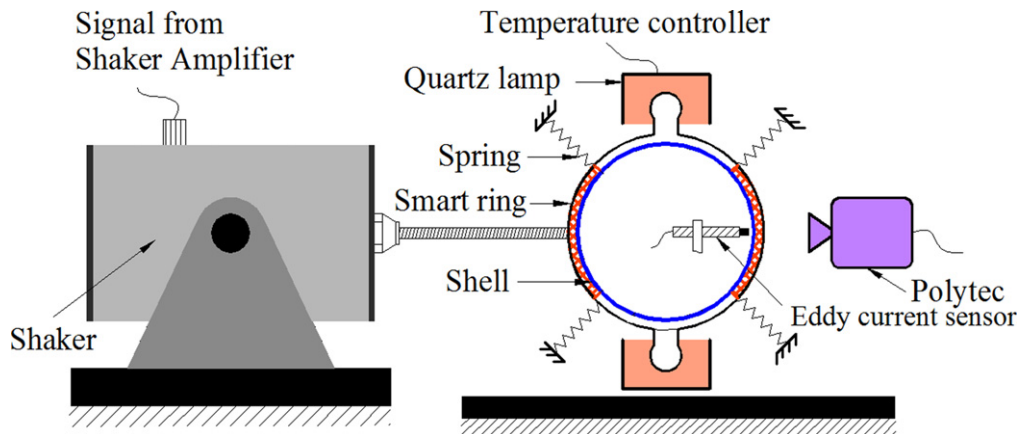
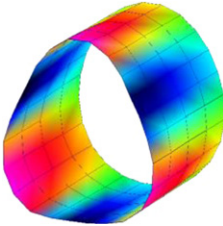
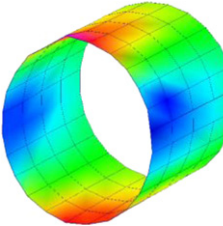
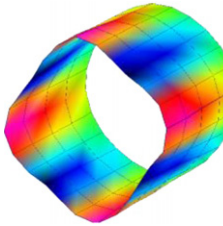


Figure 7. Schematic diagram of the test system.

Table 1 Natural frequency and mode shape of the shell (unit: Hz).

Method	Natural frequency and mode shape		
	$m = 3, n = 1$	$m = 2, n = 1$	$m = 4, n = 1$
			
Hammering method	363.2	456.2	530.1

5. Results and discussion

5.1. Inherent properties of the shell

5.1.1. Without the smart ring. A modal experiment was built to detect the inherent properties of the test shell using the hammering method.

Table 1 shows that there are three natural frequencies with the mode shapes $m = 3, 2$ and 4 within 600 Hz. As a result of the large spacing between the first three natural frequencies of the shell, the feasibility of the experiment is guaranteed.

5.1.2. With the smart ring. An inherent properties experiment was carried out with the smart ring kept tightened by heating. Meanwhile the other two kinds of smart rings with steel or MR inner ring were also tested.

Figure 9 and table 2 illustrate the transfer function and modal frequencies of the shell with the smart ring. For the steel–MR smart ring, all three modal frequencies are observed to have decreased. This decrement is on account of the added mass and damping of the ring, while the influence of the added stiffness due to the constraint of the smart ring is smaller. In addition to the frequency 330 Hz ($m = 3$), a new frequency 351 Hz appears with the same mode shape, which is considered to be as a result of the impact of the asymmetry of constraint of the smart ring. Furthermore, the amplitude of all three resonant frequencies is reduced significantly. Through comparison with the other two types of smart rings, it can be concluded that the steel smart ring possesses good properties both in frequency adjustment and amplitude constraint, while the MR smart ring is limited due to the low stiffness of the MR sheet.

5.2. Vibration response control

5.2.1. Excitation with variable frequency. The simple control strategy that the smart ring stays in constriction at all times is adopted to control the vibration due to a variable frequency excitation which primarily represents a predictable process across the resonance. An excitation (frequency range 300 – 600 Hz, sweeping frequency speed 25 Hz s^{-1}) was

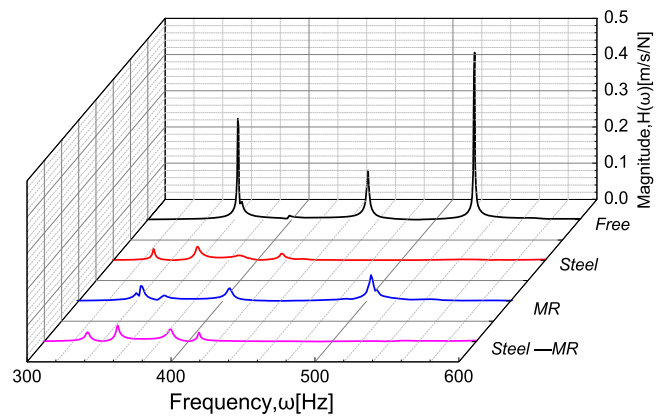


Figure 9. The transfer function for point P versus different kind of smart rings.

Table 2. Frequency of shell versus different kind of smart ring (units: Hz).

Inner ring	Frequency		
	$m = 3$	$m = 2$	$m = 4$
Free	363	453	527
Steel	328/358.5	387	418
MR	334	405	503
Steel–MR	330/351	388	407

applied to the shell by the shaker after the recovery force of the SMA actuators reached the maximum and were stable.

Figure 10 shows the amplitude response of the shell versus time while free (in black), and with the steel–MR smart ring (in red). The shell mainly goes through three resonance frequencies with mode shapes $m = 2, 3$ and 4 . Without the smart ring, the amplitude peak can reach a high level and the amplitude of the mode shape ($m = 2$) is the biggest, equal to 1.6×10^{-5} m. After the temperature of the actuators stabilizes at 90 °C, the amplitude of all three peaks was decreased to a great degree and the maximum amplitude of the three peaks lowered to 6.1×10^{-6} m. The resonance peaks appear much earlier than in the free situation, giving a strong indication that the smart ring is capable of frequency

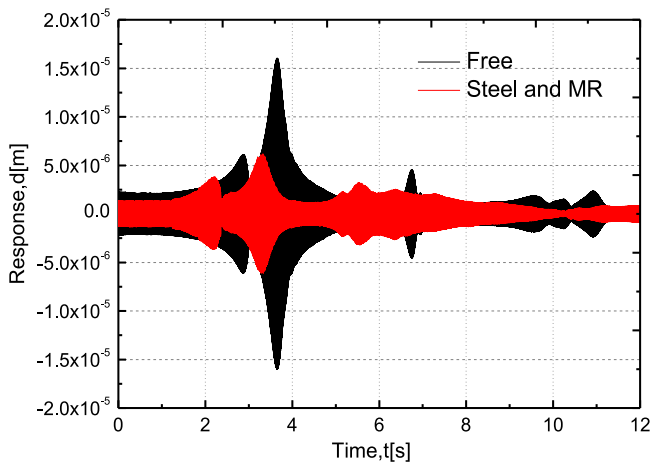


Figure 10. The amplitude response of the shell under variable frequency excitation.

adjustment. Another point to note is that the amplitude of the shell in a non-resonance region is much lower than that when the shell is free from constraint, which shows that the smart ring can always perform well in controlling the vibration of the shell for the whole frequency range.

The experiment was repeated using the same settings with each of the other two rings replacing the smart ring. In order to compare the vibration control effect of the three kinds of smart rings, the envelope curve of the response is obtained and the biggest amplitude of response without a smart ring is set as the reference. The vibration control effect is illustrated in figure 11, which shows declines in all of the resonance amplitudes, especially for the tests with the smart rings with steel and steel–MR inner rings. To be precise, the amplitude decrement for the two smart rings exceeds 60% and that for the steel–MR smart ring is 61.5%.

5.2.2. Excitation with fixed frequency. Considering that the resonance of the shells mostly takes place with unpredictable excitations during operation, the control strategy of heating the smart ring once resonance is introduced indicates that a process of separation–contact–pressure happens between the shell and smart ring. Taking the mode shape ($m = 3$) as an instance, the shell was separated from the smart ring at the beginning and then excited to resonate. Afterwards the SMA actuators were heated to make the smart ring shrink until the response of the shell was stable. The responses of the shell and smart ring are shown in figures 12 and 13 respectively. Then, the fast Fourier transform (FFT) calculation of the response of the shell for the whole test process is illustrated in figure 14(a) while that after control is depicted in figure 14(b).

As shown in figures 12 and 13, the control procedure can be separated into four stages. During the first stage, the shell, which resonated with an amplitude of $5 \mu\text{m}$ due to the excitation, is separated from the smart ring. The contact between the shell and ring happened during the second stage, which made the amplitude of the shell rise by 4.1%. The smart ring started to shrink once it was heated and touched the

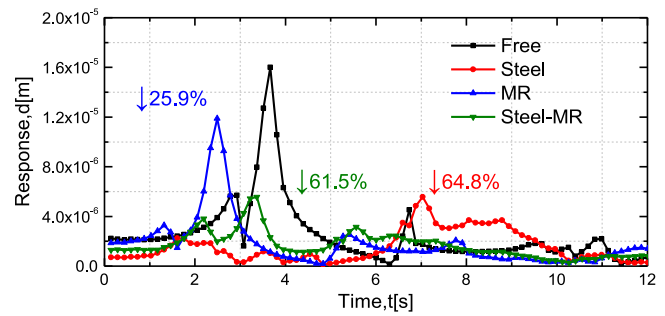


Figure 11. The envelope curves of the response for shells with different smart rings.

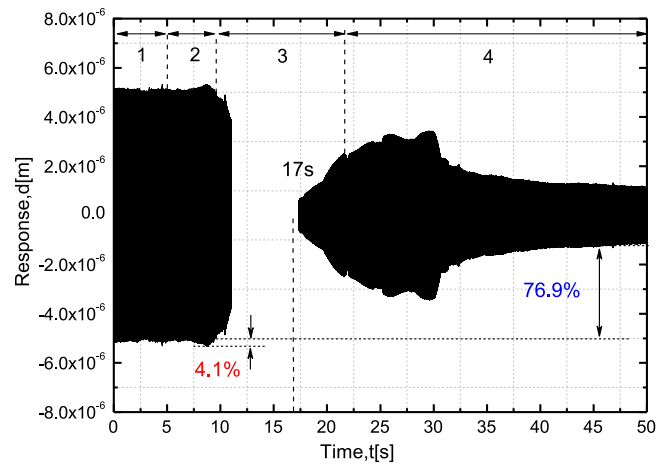


Figure 12. Amplitude response of the shell with fixed-frequency excitation versus time.

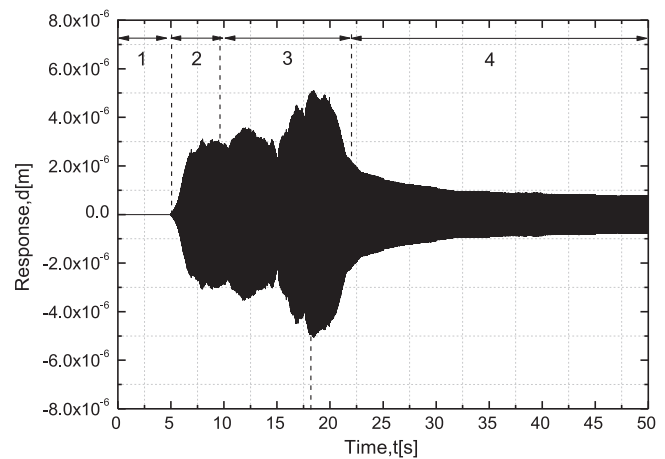


Figure 13. Amplitude response of the smart ring with fixed-frequency excitation versus time.

shell at the 6th second. A basic and small $\times 1.5$ frequency can be seen in figure 14(a), suggesting that the high efficiency of the damping and impact energy absorption of the MR sheet can restrain the nonlinear vibration of the shell due to its contact and rubbing with the smart ring. In the third stage, the inherent characteristics of the shell and smart ring are altered

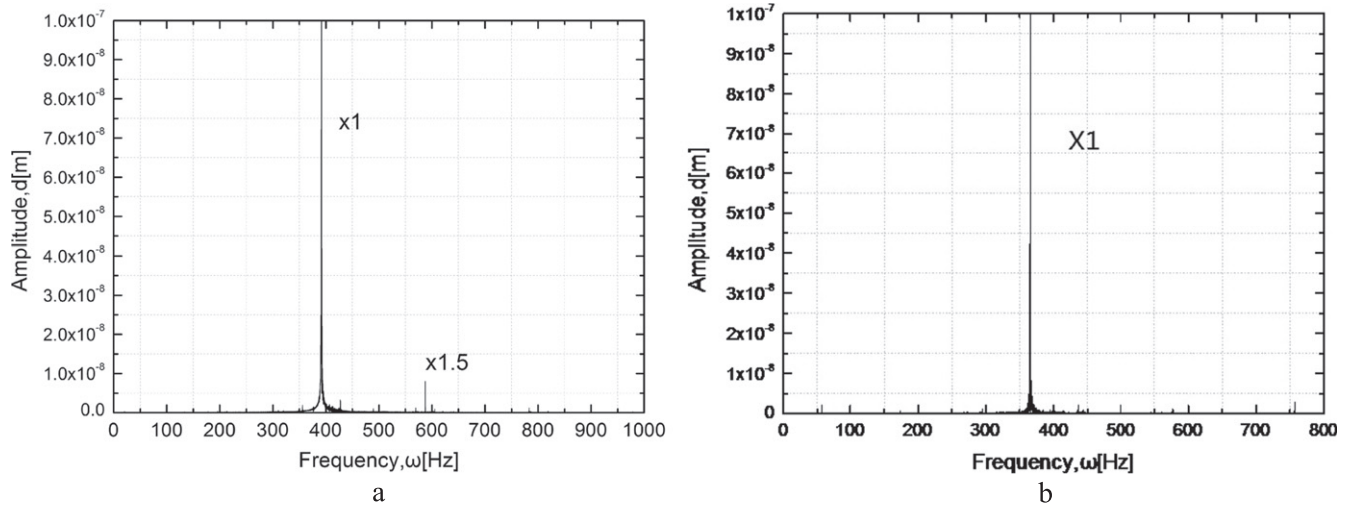


Figure 14. FFT calculation of amplitude of the shell, (a) the whole process, (b) after control.

due to the interaction between them. According to figures 12 and 13, the amplitude of the shell dropped greatly and reached a minimum at about the 17th second, while synchronously, the vibration of the ring increased significantly, which is explained by the smart ring working as a dynamic absorber absorbing the vibration of the shell during this stage. Finally, during the fourth stage, the vibration amplitude of the shell tended to be stable and then decreased to 76.9% of that before control, with the pressure from the ring increasing and staying stable at the maximum. In addition, the amplitude of the smart ring kept to a low value, benefiting from the interaction between the two components.

Figure 15 shows the response of the shell versus time while the SMA actuators were heated and then cooled. The result demonstrates that the response control for the shell is achieved with an amplitude decline of 78.0% after experiencing rubbing and vibration absorption, and the restorability of the vibration characteristics of the shell is verified with a slight decrement of 1.3% in amplitude when the smart ring is cooled to room temperature.

The experiment was repeated with the other two smart rings replacing the smart ring. The results are presented in table 3 (details are given in figures A1–A4 in the appendix).

For the steel smart ring, although the final amplitude of the shell can be decreased by 68.8%, the stability of the system is poor because the rubbing between the ring and shell, brought a nonlinear vibration with a large frequency multiplication and fractional frequency to the shell. The MR smart ring performed well with regard to stability, but the control effect is not good enough compared with the other two kinds of rings. Above all, the steel–MR smart ring behaves best because of its high stability, rapid effectiveness, and large amplitude decrement.

In conclusion, by fixing a slice of MR sheet to the steel ring, the steel–MR smart ring combines the advantages of the other two kinds of smart rings, which makes it possible to efficiently achieve vibration control through frequency adjustment, damping and amplitude constraint.

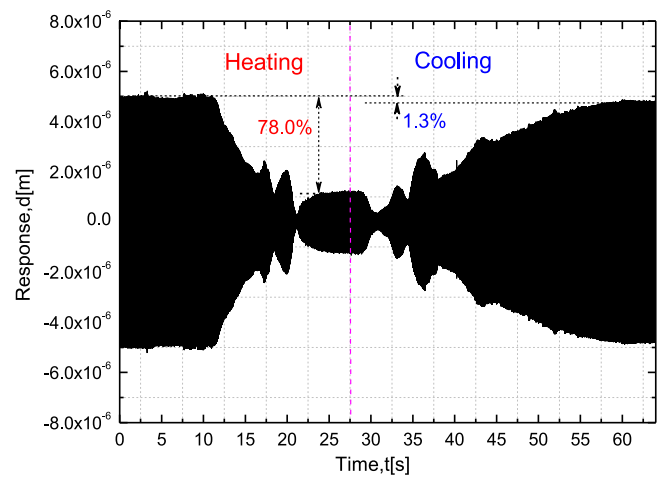


Figure 15. Amplitude response of the shell with fixed-frequency excitation during heating and cooling.

Table 3. The effect of vibration control versus different smart rings.

Smart ring	I_{Ac} ^a (%)	D_{As} ^a (%)	Full time frequency domain signal
Steel–MR	4.1	76.9	$\times 1, \times 1.5$
Steel	27.2	68.8	$\times 0.5, \times 1, \times 1.5, \times 2$
MR	4.43	41.0	$\times 1, \times 2$

^a I_{Ac} is defined as the amplitude increment during the contact while D_{As} is the amplitude decrement after stabilizing.

5.3. Vibration isolation

Vibration isolation is another challenge for aero-engine casings which always play a role as a connection to transfer the vibration outward. Due to the complexity of the excitation usually resulting from rubbing or airflow excitation, the requirement for the casing to isolate vibrations must be satisfied. Impact and random loads are two kind of typical excitation for the casing. Given its effectiveness in the former experiment, the steel–MR smart ring was selected as the object to investigate with respect to its ability to isolate the

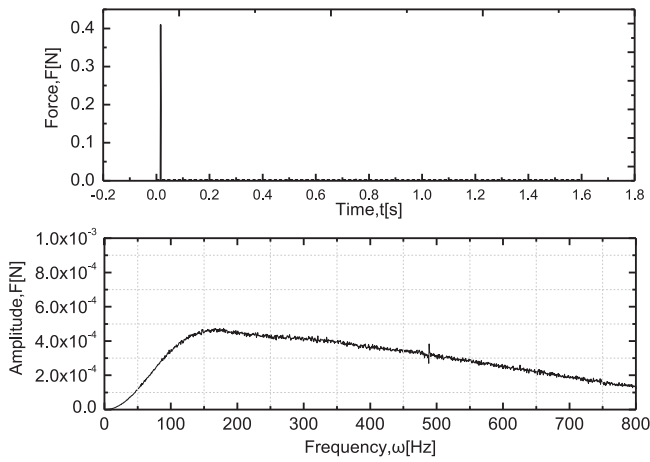


Figure 16. Impact signal both in time and frequency domain.

vibration excited by impacts or random loads. Two parameters were defined herein, namely the displacement transmissibility T_d and amplitude impedance I_d . T_d is defined as the amplitude ratio of two measured points, while I_d is the ratio of the amplitude of the measured point to the force amplitude of the excited point.

5.3.1. Impact load excitation. Impact loads, such as rubbing between blades and casing, are common loads for aero-engine casings and in figure 16 both the time and frequency domains are shown for the experiment.

Taking points 3 and 8 as an example, the curves of the time domain of the two points are illustrated in figure 17. Before control, the response of the two points attenuates slowly and maintains a high amplitude level, however, the responses get smaller and reduce to the minimum within 0.5 s when the smart ring is heated. The T_d of point 8 to 3 is 0.32 and the I_d of point 8 is $96\,564\text{ N m}^{-1}$ while the two parameters are changed to 0.18 and $152\,378\text{ N m}^{-1}$ after control, suggesting the availability of the smart ring which can have a significant influence on the ability of the shell in vibration isolation by increasing the damping and stiffness.

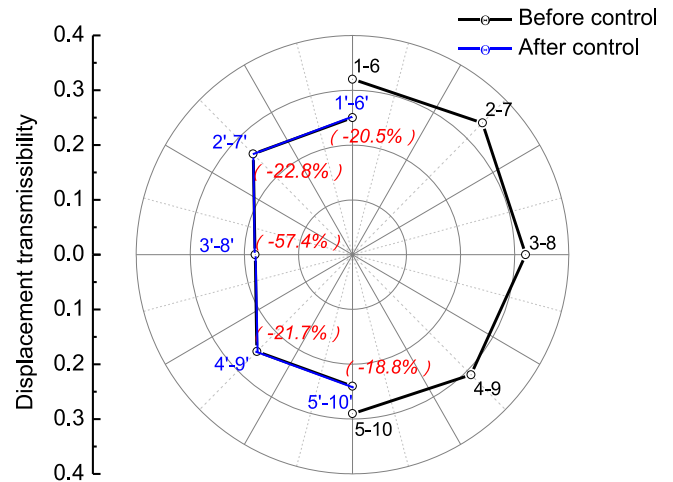
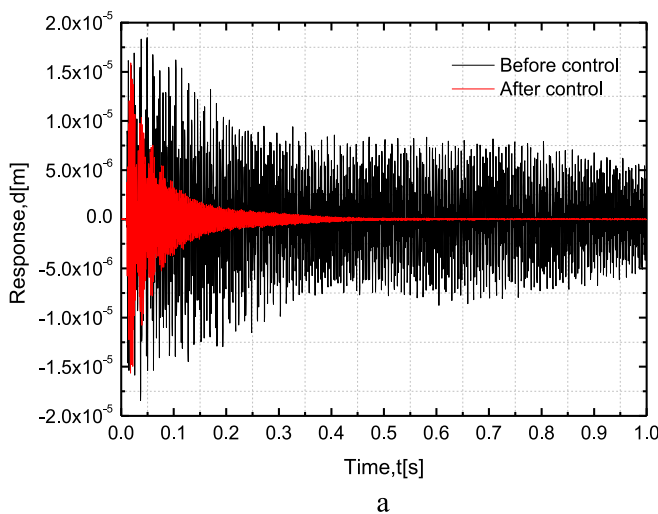


Figure 18. T_d of measure points with the same phase in circumference before and after control.

Figures 18 and 19 illustrate the T_d value of the measure points with the same phase in circumference and the I_d of all points to their excited points respectively (the values are presented in tables A1 and A2 in the appendix). Resulting from the even distribution on the circumference, the results show a symmetrical distribution. The values of T_d are all reduced by around 20%; however, this is decreased by 57.4% for points 8 to 3 because points 8 and 3 are placed in the same phase in the circumference with the center of the inner ring. At the same time, the I_d value of all points increased to some degree and the increment enlarges as the distance between the measuring point and the center of inner ring decreases, especially for points 6–10 which are distributed on the right side of the smart ring as shown in figure 8. The I_d value of point 8 increased the most, by 57.8%.

The satisfactory vibration isolation performance of the smart ring with sectional inner rings under impact loads is validated and the performance possesses a symmetrical distribution. Therefore, it is pragmatic to improve the effect of the smart ring by extending the area of the inner ring or increasing the number of smart rings.

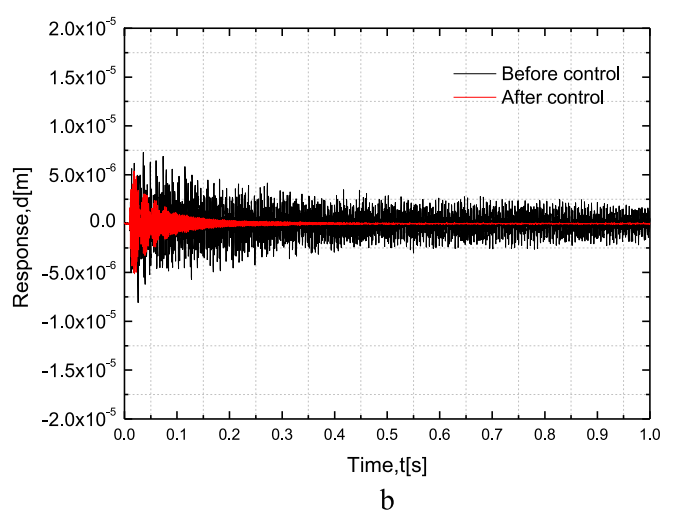


Figure 17. Comparison between the responses before and after control: (a) point 3; and (b) point 8.

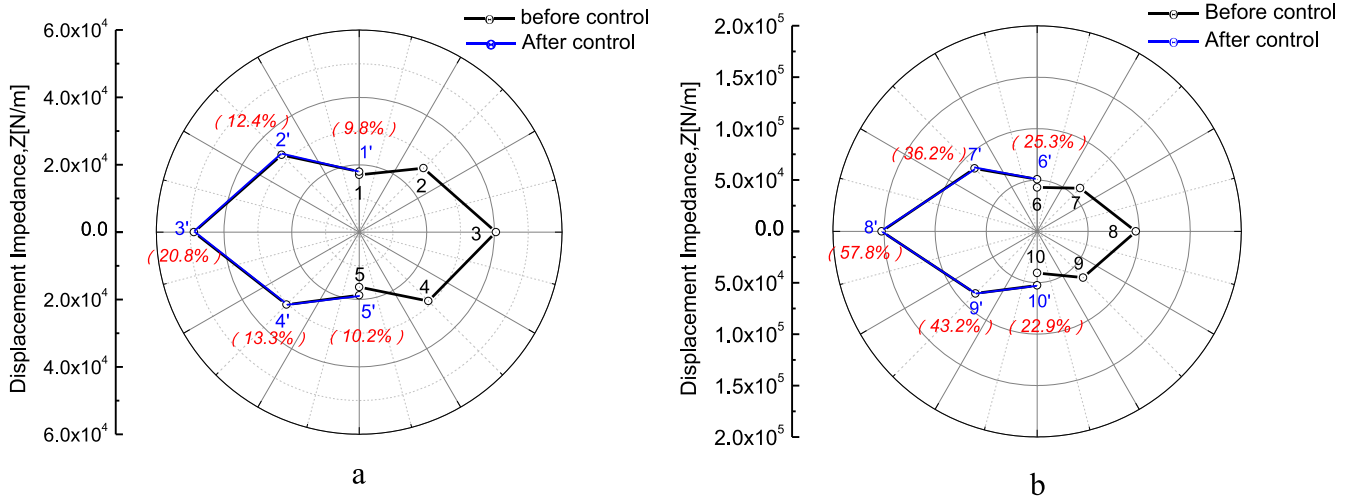


Figure 19. I_d of measured points to excited points before and after control, (a) for 1–5 points, and (b) for 6–10 points.

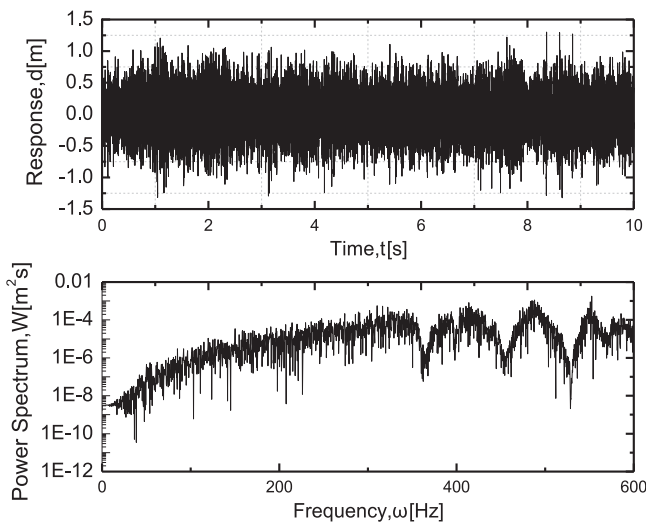


Figure 20. The time history curve and power spectrum of the random signal.

5.3.2. *Random load excitation.* Acoustic excitation in an aero-engine is always generated by combustion or high speed airflow and behaves like a random excitation, and is simulated by a white noise signal in the experiment. The time domain curve and power spectrum of the random signal are shown in figure 20.

Figures 21 and 22 represent the time domain curve and power spectrum of the signals from points 3 and 8. As we can see, the amplitude responses of both points are reduced. Furthermore, the overall root-mean-square value of the amplitude response of the two points are decreased by 29.2% and 31.6%, respectively (listed in table 4). However, the vibration decrement is concentrated in the resonance region of the shell (shown in the power spectrum plots).

The decrement of the T_d value for points at the same position circumferentially can reach over 10%, especially for points 8 to 3, with a value reaching 38.7% (see table 5). It can be said that the smart ring not only decreases the vibration of the shell itself but also improves the capability for vibration isolation by applying added damping and stiffness to the shell.

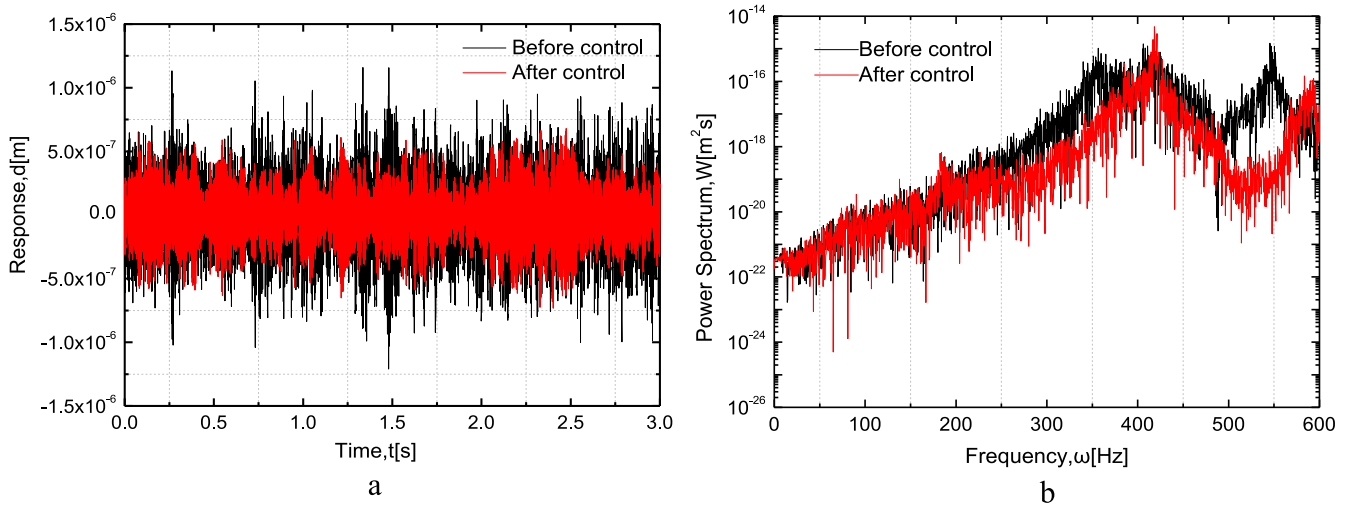


Figure 21. Signal from point 3; (a) time history curve, and (b) power spectrum.

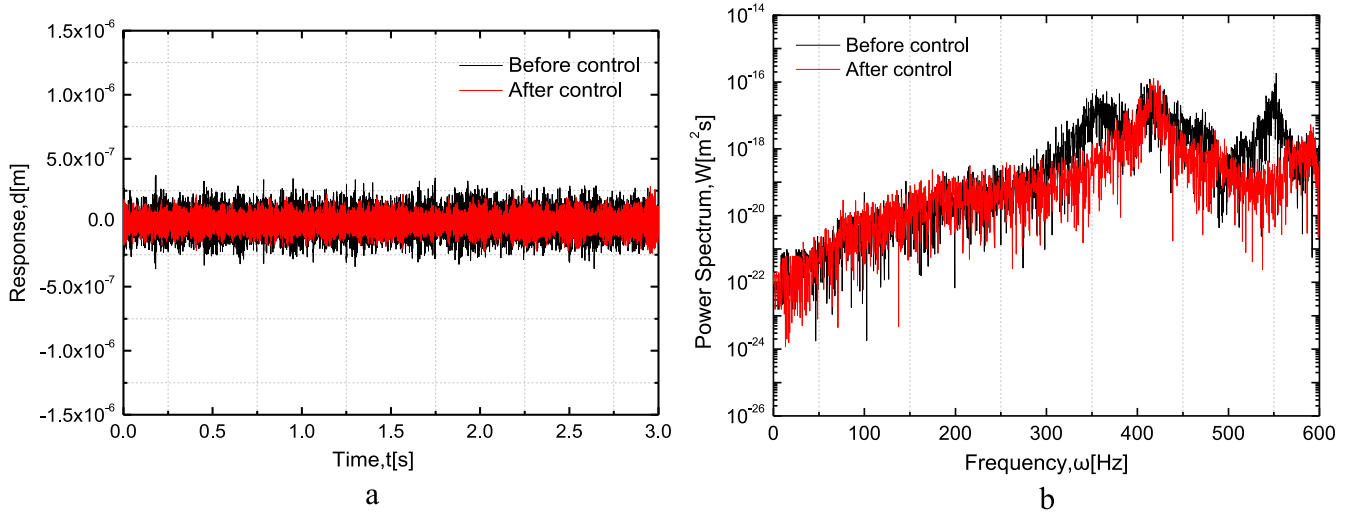


Figure 22. Signal from point 8; (a) time history curve, and (b) power spectrum.

Table 4. The overall root-mean-square value of amplitude response for points 3 and 8.

Points	Before control (m)	After control (m)	Decrement %
3	2.95 E-07	2.09 E-07	29.2
8	9.28 E-08	6.35 E-08	31.6

6. Conclusions

This paper introduces the manufacture and testing of a smart ring with SMA actuators placed symmetrically. The SMA actuators are fabricated using Ti50Ni41Cu9 shape memory alloy plates which have been through heat setting and two-way shape memory training. Evidence of vibration control and isolation are given by heating and/or cooling the smart ring during shell vibration. It is possible to draw the following conclusions:

- (1) Due to the temperature dependence and shape memory effect of the SMA actuators, the smart ring yields a 1280 N recovery force applied on the shell when heated at 90 °C. The natural frequency of the test shell with a steel-MR smart ring varies from 363 Hz ($m = 3$), 453 Hz ($m = 2$), and 527 Hz ($m = 4$) to 330 Hz, 388 Hz, and 407 Hz, respectively. In addition, a new frequency 351 Hz with mode shape ($m = 3$) is introduced by the asymmetry of the smart ring. These are more than acceptable values for amplitude decrements reaching over 50%, showing the interesting smart ring properties of frequency adjustment and amplitude constraint.
- (2) The steel-MR smart ring not only shows good stability and quick effectiveness in vibration control for the test shell, but observably eliminates the nonlinear vibration

Table 5. Comparison of the T_d of measure points at the same position circumferentially.

Number of points	Before control	After control	Decrement %
1-6	0.42	0.37	11.9
2-7	0.26	0.30	15.3
3-8	0.28	0.38	38.7
4-9	0.33	0.37	12.9
5-10	0.50	0.55	12.0

characteristics due to contact and rubbing occurring between the ring and shell during the heating process. As for the fixed-frequency excitation experiment, the amplitude decrement can reach 76.9% and the frequency domain curves just include a basic and small $\times 1.5$ frequency.

- (3) The smart ring possesses an excellent ability in isolation of transient vibration resulting from impact or random loads. The mechanical impedance of the shell enlarges greatly on account of the effect of the amplitude constraint of the steel ring and high damping of the MR sheet. With regard to impact loads, the value can reduce by 57.4% at most while the value is 38.7% for random excitation, suggesting the feasibility of using the steel-MR smart ring for potential applications of vibration isolation in the casing of aero-engines.

Acknowledgments

This work was financially supported by the National Natural Science Foundation of China (Grant nos. are 51475021 and 51475023).

Appendix

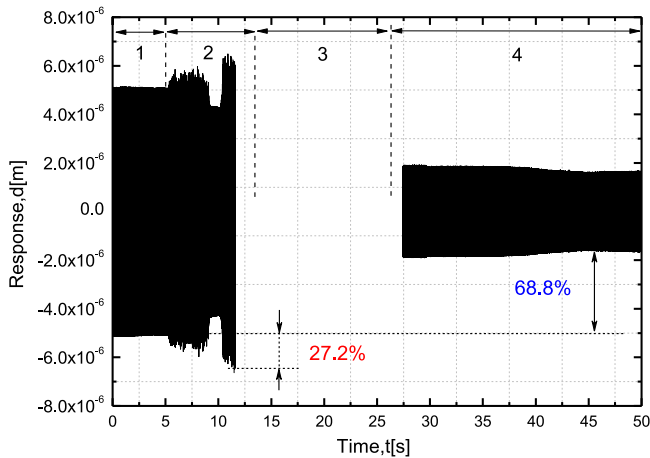


Figure A1. Amplitude response of the shell with fixed-frequency excitation versus time with the steel smart ring.

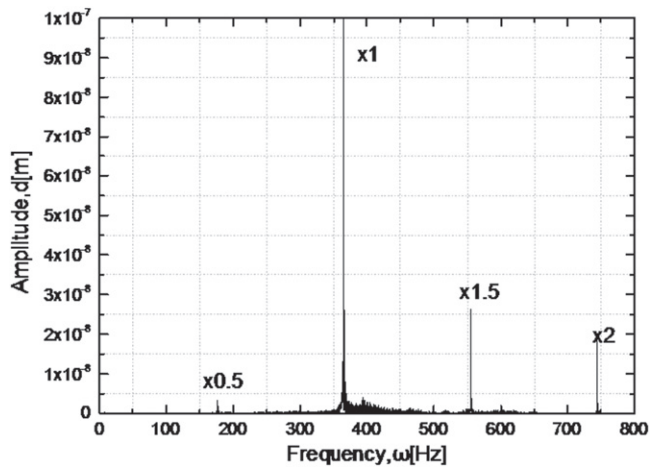


Figure A2. FFT calculation of the amplitude of the shell during the whole process with the steel smart ring.

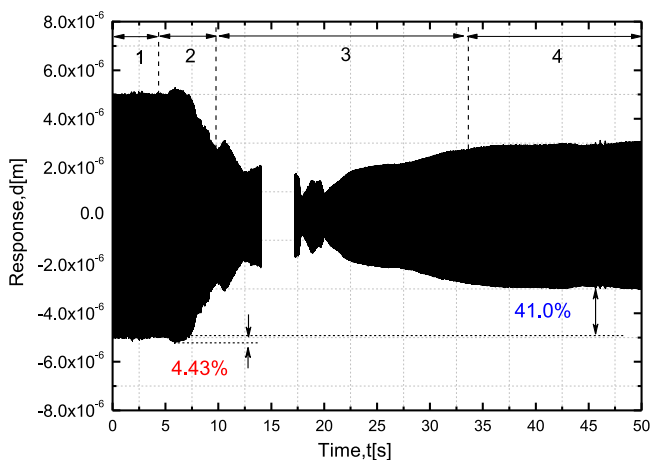


Figure A3. Amplitude response of the shell with fixed-frequency excitation versus time with the MR smart ring.

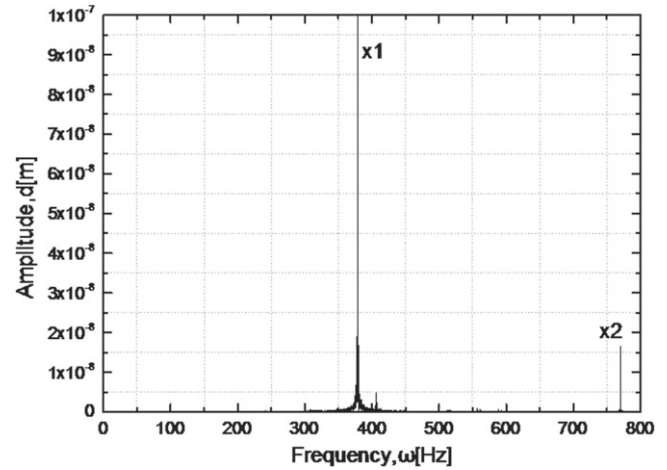


Figure A4. FFT calculation of the amplitude of the shell during the whole process with the MR smart ring.

Table A1. Comparison of displacement transmissibility of points before and after control.

Points	Before control	After control	Decrement %
1-6	0.32	0.25	20.5
2-7	0.34	0.26	22.8
3-8	0.32	0.18	57.4
4-9	0.31	0.25	21.7
5-10	0.29	0.24	18.8

Table A2. Comparison of amplitude impedance of points before and after control.

Points	Before control (N m ⁻¹)	After control (N m ⁻¹)	Increment %
1	16 327	17 927	9.8
2	28 872	32 452	12.4
3	40 434	48 844	20.8
4	26 864	30 436	13.3
5	17 014	18 749	10.2
6	40 434	50 663	25.3
7	63 667	86 714	36.2
8	96 564	152 378	57.8
9	59 627	85 385	43.2
10	42 654	52 421	22.9

References

[1] Housner G W, Bergman L A, Caughey T K, Chassiakos A G, Claus R O, Masri S F, Skelton R E, Soong T T, Spencer B F and Yao J T P 1997 Structural control: past, present and future *J. Eng. Mech.* **123** 897-971

[2] Liu W, Tomlinson G R and Rongong J 2005 The dynamic characterisation of disk geometry particle dampers *J. Sound Vib.* **280** 849-61

[3] Petrov E 2011 Reduction of forced response levels for bladed disks by mistuning: overview of the phenomenon *J. Eng. Gas Turbines Power* **133** 072501

- [4] Schwingshackl C W, Petrov P and Ewins D J 2012 Effects of contact interface parameters on vibration of turbine bladed disks with underplatform dampers *J. Eng. Gas Turbines Power* **134** 032507
- [5] Petrov E and Ewins D J 2006 Effects of damping and varying contact area at blade-disk joints in forced response analysis of bladed disk assemblies *J. Turbomach.* **128** 403–10
- [6] Lim T C 2014 Buckling and vibration of circular auxetic plates *J. Eng. Mater. Technol.* **136** 021007
- [7] Wong W O, Tang S L, Cheung Y L and Cheng L 2007 Design of a dynamic vibration absorber for vibration isolation of beams under point or distributed loading *J. Sound Vib.* **301** 898–908
- [8] Zheng H, Cai C, Pau G S H and Liu G R 2005 Minimizing vibration response of cylindrical shells through layout optimization of passive constrained layer damping treatments *J. Sound Vib.* **279** 739–56
- [9] Abbas H, Hai H, Rongong J and Xing Y 2014 Damping performance of metal swarfs in a horizontal hollow structure *J. Mech. Sci. Technol.* **28** 9–13
- [10] Tan P and Zhou F 2007 Structural active variable stiffness-damping control system and its optimal design *J. Architect. Civil Eng.* **24** 6–12
- [11] Chen M, Pan Y, Liu B and Bai H 2011 Research on electromagnetic support for supporting mechanical system by variable stiffness *China Mech. Eng.* **22** 1862–6
- [12] Chang I J M and Soong T 1980 Optimal controller placement in modal control of complex systems *J. Math. Anal. Appl.* **175** 340–58
- [13] Sandler B 1980 Adaptive mechanisms (automatic vibration control) *J. Sound Vib.* **73** 161–75
- [14] Nagaya K and Takeda S 1987 Active control method for passing through critical speeds of rotating shafts by changing stiffness of the supports with use of memory metals *J. Sound Vib.* **113** 307–15
- [15] Loh C H and Ma M J 1996 Control of seismically excited building structures using variable damper systems *Eng. Struct.* **18** 279–87
- [16] Jani J M, Leary M, Subic A and Gibson M A 2014 A review of shape memory alloy research, applications and opportunities *Mater. Design* **56** 1078–113
- [17] Hassan M R, Scarpa F and Mohamed N A 2004 Shape memory alloys honeycomb: design and properties *Proc. SPIE* **5387** 557–64
- [18] Hassan M R, Scarpa F, Ruzzene M and Mohammed N A 2008 Smart shape memory alloy chiral honeycomb *Materials Science and Engineering A* **481** 654–7
- [19] Rossiter J, Scarpa F, Takashima K and Walters P 2012 Design of a deployable structure with shape memory polymers *Proc. SPIE* **8342** 83420Y
- [20] Jacobs S, Coconnier C, DiMaio D, Scarpa F, Toso M and Martinez J 2012 Deployable auxetic shape memory alloy cellular reflector demonstrator: design, manufacturing and modal testing *Smart Mater. Struct.* **21** 075013
- [21] Ölander A 1932 An electrochemical investigation of solid cadmium–gold alloys *J. Am. Chem. Soc.* **54** 3819–33
- [22] Buehler W J, Gilfrich J V and Wiley R C 1963 Effect of low-temperature phase changes on the mechanical properties of alloys near composition TiNi *Appl. Phys.* **34** 1475–7
- [23] Furuya Y 1996 Design and material evaluation of shape memory composites *J. Intell. Mater. Syst. Struct.* **7** 321–30
- [24] Butera F, Coda A and Vergani G 2007 Shape memory actuators for automotive applications *Nanotec IT Newsletter Roma: AIRI/Nanotec IT* 12–6
- [25] Mieloszyk M, Krawczuk M, Zak A and Ostachowicz W 2010 An adaptive wing for a small-aircraft application with a configuration of fibre Bragg grating sensors *Smart Mater. Struct.* **19** 085009
- [26] Hartl D J, Lagoudas D C, Calkins F T and Mabe J H 2010 Use of a Ni60Ti shape memory alloy for active jet engine chevron application: I. Thermomechanical characterization *Smart Mater. Struct.* **19** 015020
- [27] Hartl D J, mooney J T, Lagoudas D C, Calkins F T and Mabe J H 2010 Use of a Ni60Ti shape memory alloy for active jet engine chevron application: II. Experimentally validated numerical analysis *Smart Mater. Struct.* **19** 015021
- [28] Oehler S D, Hartl D J, Lopez R, Malak R J and Lagoudas D C 2012 Design optimization and uncertainty analysis of SMA morphing structures *Smart Mater. Struct.* **21** 094016
- [29] Yuse K, Kikushima Y and Xu Y 2002 Experimental considerations on fabrication of a smart actuator for vibration control using shape memory alloy *Proc. SPIE* **4697** 382–92
- [30] Suzuki Y and Kagawa Y 2010 Active vibration control of a flexible cantilever beam using shape memory alloy actuators *Smart Mater. Struct.* **19** 5014–22
- [31] Chen Y 2010 Application of shape memory alloys to control the vibration of solar panels *Mech. Eng. Automat.* **2** 172–4
- [32] Zhang D, Scarpa F, Ma Y, Hong J and Mahadik Y 2014 Dynamic mechanical behavior of nickel-based superalloy metal rubber *Mater. Des.* **56** 69–77
- [33] Ma Y, Zhang Q, Zhang D, Scarpa F, Liu B and Hong J 2014 A novel smart rotor support with shape memory alloy metal rubber for high temperatures and variable amplitude vibrations *Smart Mater. Struct.* **23** 125016
- [34] Li H, Mao C and Qu J 2008 Experimental and theoretical study on two types of shape memory alloy devices *Earthquake Eng. Struct. D* **37** 407–26
- [35] Zhang Y and Zhu S 2007 A shape memory alloy based reusable hysteretic damper for seismic hazard mitigation *Smart Mater. Struct.* **16** 1603–13
- [36] Wickramasinghe K, Tomlinson G R and Rongong J 2015 *In situ* observation of NiTi transformation behaviour: a micro–macro approach *Experimental and Applied Mechanics* vol 6 (New York: Springer-Verlag) pp 13–20
- [37] Zotov N, Marzynkevitch V and Mittemeijer E J 2014 Evaluation of kinetic equations describing the martensite–austenite phase transformation in NiTi shape memory alloys *J. Alloys Compd.* **616** 385–93
- [38] Roh J, Han J and Lee I 2005 Finite element analysis of adaptive inflatable structures with SMA strip actuator *Proc. SPIE* **5764** 460–71
- [39] Yang N, Peng W, Yan M, Wang W and Shi H 2013 Influence of aging time on mechanical properties and microstructures of FeNiAlTi shape memory alloy *Acta Phys. Sin.* **62** 158106
- [40] Karhu M and Lindroos T 2010 Long-term behaviour of binary Ti–49.7 Ni (at.%) SMA actuators—the fatigue lives and evolution of strains on thermal cycling *Smart Mater. Struct.* **19** 115019
- [41] Huang S, Leary M, Ataalla T, Probst K and Subic A 2012 Optimisation of Ni–Ti shape memory alloy response time by transient heat transfer analysis *Mater. Design* **35** 655–63
- [42] Ma Y, Wang M, Yang X, Zhang D and Hong J 2015 Experimental investigation on the vibration tuning of a beam with shape memory alloy *Proc. ASME 2015 Turbo Expo (Montreal)* GT2015–42262
- [43] Hong J, Chen L, Ma Y, Tomlinson G R and Rongong J 2013 Hysteretic properties of metal rubber particles *P. I. Mech. Eng. C-J. Mech.* **227** 693–702
- [44] Hong J, Liu B, Zhang D and Ma Y 2012 Shape memory effect and hysteresis behavior of shape memory alloy metal rubber, *ASME Conf. (Copenhagen)* GT2012–69244

- [45] Ma Y, Zhu H, Zhang D, Liu B and Hong J 2013 Experimental investigation on shape memory alloy metal rubber *Sci. China Technol. Sc.* **56** 1949–55
- [46] Zhang D, Scarpa F, Ma Y, Boba K, Hong J and Lu H 2013 Compression mechanics of nickel-based superalloy metal rubber *Mater. Sci. Eng. A* **580** 305–12
- [47] Kerwin J 1959 Damping of flexural waves by a constrained viscoelastic layer *J. Acoust. Soc. Am.* **31** 952–62
- [48] Baz A and Ro J 1996 Vibration control of plates with active constrained layer damping *Smart Struct. Mater.* **5** 272
- [49] Kumar N and Singh S 2010 Experimental study on vibration and damping of curved panel treated with constrained viscoelastic layer *Compos. struct.* **92** 233–43
- [50] DeHaven J and Tzou H 2008 Forced response of cylindrical shells coupled with nonlinear shape-memory-alloy (SMA) actuators regulated by sinusoidal and saw-tooth temperature profiles *J. Eng. Math.* **61** 301–13
- [51] Li H, Li H and Tzou H 2013 Vibration control of cylindrical shell panel with shape memory alloy actuators *ASME Conf. (Portland, OR)* DETC2013-12788
- [52] Zarzour M and Vance J 2000 Experimental evaluation of a metal mesh bearing damper *J. Eng. Gas Turbines Power* **122** 326–9
- [53] Al-Khateeb E and Vance J 2001 Experimental evaluation of a metal mesh bearing damper in parallel with a structural support, *ASME Turbo Conf. (New Orleans, LA)* GT2001-0247
- [54] Ma Y, Wang H, Li H and Hong J 2008 Study on metal rubber material's characteristics of damping and sound absorption, *ASME Conf. (Berlin)* GT2008-50961